Quantifying multiple electromagnetic properties in EMI surveys: A case study of hydromorphic soils in a volcanic context – The Lac du Puy (France)

François-Xavier Simon, Mathias Pareilh-Peyrou, Solène Buvat, Alfredo Mayoral, Philippe Labazuy, Karim Kelfoun, Alain Tabbagh

Quantifying multiple electromagnetic properties in EMI surveys: a case study of hydromorphic soils in a volcanic context – the Lac du Puy (France)

François-Xavier Simon[1], Mathias Pareilh-Peyrou[2], Solène Buvat[2], Alfredo Mayoral[3], Philippe Labazuy[2], Karim Kelfoun[2], Alain Tabbagh[4]

[1]: Institut National de Recherches Archéologiques Préventives, Laboratoire Chrono-Environnement, UMR 6249, F-25000, Besançon, France, francois-xavier.simon@inrap.fr

[2]: Université Clermont Auvergne, CNRS, IRD, OPGC, Laboratoire Magmas et Volcans, F-63000 Clermont-Ferrand, France

[3]: CNRS, Université Clermont Auvergne, GEOLAB, F-63000 Clermont-Ferrand, France

[4]: Sorbonne Université, CNRS, EPHE, Métis, 4 place Jussieu F-75252, Cedex 05 Paris, France

Abstract

We used two different loop-loop electromagnetic induction (EMI) devices to determine the 3D geometry and morphology of the pedo-sedimentary filling and underlying basaltic bedrock of a former wetland in a volcanic soil area, the Lac du Puy depression (Auvergne, France). Electrical conductivity (or resistivity) is usually sufficient for environmental and soil science applications, but the local volcanic context of the survey area results in high values of magnetic susceptibility and possible electrical polarization effects. Therefore we investigated the roles of the four properties: electrical conductivity, magnetic susceptibility, magnetic viscosity and dielectric permittivity. We created models using these four properties for the two coil configurations of each device in order to assess the degree to which each of the properties contributed to the recorded electromagnetic signal. The results show that electrical conductivity controls the quadrature component of the secondary field response but that it can be affected by high values of magnetic viscosity, while magnetic susceptibility controls the in-phase

component. Moreover, the low frequencies imply a limited contribution of dielectric permittivity to the in-phase component, except in the cases of higher permittivity or frequency values or greater inter-coil separation. Based on these observations, we propose a way to map the apparent properties from field measurements. We then carried out a 1D inversion, first by considering the electrical conductivity alone and secondly by taking all the electromagnetic properties into account. The results show that there is a marked contrast in the complex magnetic susceptibility between the sedimentary in-fill and the border of the Lac de Puy depression, (stronger than for the electrical conductivity), and that permittivity is unlikely to have a significant influence. The shape and nature of the sedimentary in-fill was thus considerably refined by the second inversion results based on the three other properties. These data, combined with litho-stratigraphic observations from a previous study, allowed the lateral continuity and geometry of the in-fill to be assessed across the whole basin. Results are also consistent with previous interpretations of the depression as a pseudo-sinkhole, a relatively common morphology in volcanic plateaus.

Analysis of the magnetic properties also made it possible to characterize the spatial variation of some key features related to hydromorphic processes, such as clayey granularity and the development of iron oxides/hydroxides. This opens up the possibility for using new methods for rapid spatial and pedological characterization of hydromorphic soils and palaeosoils.

Key words: EMI, VLF frequency range, conductivity, magnetic susceptibility and viscosity mapping, hydromorphic soils, igneous environment

1. Introduction

Palaeosols and sedimentary layers can provide valuable records of changing Holocene environmental conditions through careful multi-proxy geo-archaeological and paleo-environmental analysis (e.g. Dotterweich, 2008; Dreibrodt et al., 2010; Henkner et al., 2017). In this context, frequency domain electromagnetic induction measurements have proven to be a useful tool in the first stages of investigation and prior to coring or trenching (Sudduth et al. 2005, Saey et al. 2008, Boaga 2017). These techniques can provide information about electromagnetic properties and make it easier to identify the nature, geometry and thickness of superficial formations and sedimentary bodies containing paleo-environmental information. Moreover, once drilling or trenching has been performed, geophysical observations calibrated with field data can be used to extrapolate stratigraphic or sedimentological observations (Bendjoudi et al. 2002, Hendrickx et al. 2002, Triantafilis and Monteiro Santos 2010, Neely et al. 2016).

In the framework of a broader geo-archaeological survey of a small pond, the Lac du Puy, situated at the top of the Puy de Corent in central France (Mayoral et al. 2018a), we used two EMI frequency domain instruments commonly used for environmental and soil studies. First the EMP400 (GSSI Ltd, Nashua, NH, USA) where the inter-coil separation, L, equals 1.2 m, and secondly the EM31 (Geonics Ltd, Mississauga, Ontario, Canada) where the inter-coil separation equals 3.66 m, both operating with frequencies close to 10 kHz. Their geometry and operating frequency define the domain of electromagnetic induction used. Here it is the Very Low Frequency (VLF, 3-30 kHz) range, in which, regardless of the type of electromagnetic transmitted signal, the electrical conductivity, σ, is the dominant cause of the underground responses. Consequently, for both instruments, only the apparent electrical conductivity is usually considered (Frischknecht et al. 1991). However, four properties are actually involved (Fig. 1): two electrical (electrical conductivity and dielectric permittivity) and two magnetic (magnetic viscosity and magnetic susceptibility):

(1) While electrical conductivity represents the global motion of electric charges at the macroscopic scale, another property, permittivity, is required to describe the electrical polarization, which is the oscillations in electrical charge at a microscopic scale (from pore or clay platelet to molecular scales). In the absence of significant changes in salinity or temperature, variations in both properties reflect variations in the granularity, mainly the clay content, or in the soil water content. Both properties can be found in the Maxwell-Ampere equation in the expression, $\sigma + i\omega\varepsilon_0\varepsilon_r$, where ω is the angular frequency, ε_0 the vacuum permittivity, ε_r the relative permittivity and $i = \sqrt{-1}$. The relative weighting of the permittivity depends on the frequency: in the low frequency (EMI) domain it can only be strong if ε_r is strong (Benech *et al.*, 2016, Simon *et al.* 2019).

(2) As the acquisition of induced magnetization by a mineral grain is not immediate, there is a delay in acquisition or loss of the induced magnetization (Dabas and Skinner 1993, McNeill 2013, Jordanova 2017). This delay is taken into account by considering that the magnetic susceptibility is a complex quantity, $\kappa = \kappa_{ph} - i\kappa_{qu}$, where κ_{ph} is the in-phase magnetic susceptibility (hereafter simply called magnetic susceptibility) and κ_{qu} is the magnetic viscosity. The magnetic viscosity depends on the size of the magnetic grains. It is strong for small single domain magnetite grains (in the [10 – 30 nm] equivalent diameter range), small for larger single domain grains (around 1 µm) and once again strong for large multi-domain grains (20 µm and greater). These magnetic properties can be used jointly to describe the degree of pedogenesis, as the quantity and size of magnetic grains are directly linked to redox processes that affect iron oxides/hydroxides. Although the presence of organic matter affects these processes (Cuenca Garcia et al. 2019), the content of iron oxides of the parent rock plays a key

role in the magnitude of soil magnetic susceptibility. In general, high magnetic susceptibility would be expected for basaltic rocks (1000 to10000 10^{-5} SI).

Frequency domain EMI apparatuses with a coil spacing of greater than 3 m and a frequency lower than 30 kHz - such as the EM31- have been used in a wide variety of environmental studies since 1979 (de Jong et al. 1979). Furthermore, over 200 papers have been published using the conductivity measurements obtained with this device (Doolittle and Brevik 2014), but to the best of our knowledge only very few studies look at the other EM property measurements for this instrument. On the other hand, in the field of archaeological prospection, where the separation between the coils remains limited, less than two meters, it has been noted that the magnetic properties play an important part in ground response (Tite and Mullins 1970, Scollar et al. 1990, Simon et al. 2015, De Smedt 2014).

In the Puy de Corent pond, the presence of basaltic rocks (basanite) underlying the depression is of particular interest in the study of magnetic properties and electrical polarization phenomena. Such rock types usually contain a high content of stable single domain magnetic grains with high susceptibility (Grison *et al.* 2015), very low viscosity and significant electrical polarizability. Therefore, the purpose of our work was to investigate the four measurable electromagnetic properties rather than using electrical conductivity alone, and to assess their relative abilities to improve interpretation of three-dimensional sedimentary infill (Triantafilis *et al.*, 2013a, Triantafilis *et al*., 2013b), well documented in Mayoral et al. 2018a but mainly based on direct and spatially limited stratigraphic observations. This non-intrusive approach provides benefits in terms of both time and resources. The raw data is collected by the two instruments and then inverted using point by point 1D modelling, considering first the electrical conductivity alone, and then incorporating the electrical conductivity, the complex magnetic susceptibility and the relative dielectric permittivity in a second round of modelling.

2. Material and methods

2-1. Study area and Stratigraphy

The study site is located on top of the Puy de Corent (621 m.a.s.l.), a volcanic plateau dominating the calcareous Limagne Plain in central France. The plateau has been shaped by erosion and topographic inversion of a 3 million year-old scoria cone and an associated basaltic lava flow formed during the Pliocene volcanism of the Massif Central (Greffier, et al., 1980; Nehlig et al., 2003). In the quasi-flat lower part of the plateau, a small circular depression of circa. 2 ha forms a wetland representing a drained pond (Fig. 2). This depression was formerly interpreted as being a secondary crater, but is more likely a pseudo-sinkhole, caused by subsidence phenomena affecting the basaltic lava flow, likely triggered by dissolution of underlying Oligocene sedimentary rocks including marls, limestones and gypsum (Mayoral et al., 2018). Litho-stratigraphic features of the Lac du Puy have already been described in detail in previous work (Mayoral et al. 2018), and are summarized here in Figure 2. The bedrock is basaltic and is formed of the Puy de Corent lava flow. The sedimentary in-fill of the basin is mainly clayey and can reach a thickness of up to 1.8 or 2 m. The lower stratigraphic units have a clay matrix which is very rich in coarse volcanic material (sand to gravel), resulting from detrital input from the plateau and local bedrock weathering and disaggregation. The middle stratigraphic units are dominated by massive, heavy clays which have undergone various phases of pedogenesis since the Neolithic, with dominant hydromorphic features (gleyic and vertic features) and rare coarse particles. The upper units are mainly clayey loams including several basaltic fragments and pottery sherds, and show Roman to present-day soil development. Magnetic susceptibility was measured on two different cores along a trench and is summarized as an average per sedimentary unit. Susceptibility values were measured with the single frequency MS2-E (Bartington Ltd, UK, 1cm spatial resolution, 2 kHz) on the fine soil fraction.

This resulted in relatively low susceptibility values (less than 50.10-5 SI), not taking into account the effect of the basaltic and sherd fragments.

2-2. Devices and survey conditions

Two different EMI devices were used on the study site. The EMP400 operates at three frequencies below 16 kHz (5, 8 and 15 kHz were selected). This instrument has one transmitting coil and one receiving coil at a distance of L=1.21 m from the transmitting coil. The coils are coplanar, and measurements can be made in either the HCP (horizontal coplanar) or the VCP (vertical coplanar), which is configured by rotating the instrument itself. The depths of investigation for the EMP400 differ between the HCP and VCP, and for the electrical and magnetic properties (Tabbagh 1986b). For the electrical properties, it is generally 0.8L in VCP and 1.5L in HCP, whereas for the magnetic ones the distances are 0.6L in VCP and 0.2L in HCP, with a change in the sign of the response for a clearance $h=0.38\ L$.

The second device, the EM31, has a coplanar configuration, a 3.66 m inter-coil separation and a single frequency of 9.8 kHz. The operator can hold the instrument at shoulder height with h=1 m clearance above the ground surface. It can also be pulled using a trolley at a lower clearance. The depths of investigation follow the same general guidelines for L as for the EMP400.

The Lac du Puy area was surveyed with the two instruments in both HCP and VCP configurations, in combination with a GNSS positioning system with a sub-decimetric accuracy in order to locate the instrument operator precisely. A profile was collected every two meters with a frequency of data collection of 1 Hz for the EM31 and 10 Hz for the EMP400. Data for both instruments and configurations were collected on October 2015, resulting in eight different independent sets of data: EM31 in HCP, EM31 in VCP, EMP400 in HCP for 5, 8 and 15 kHz and EMP400 in VCP for 5, 8 and 15 kHz. Each was resampled with the same 2 m x 2 m grid

meshing in order to enable simultaneous interpretations and inversions using these different sets.

2-3. 1D forward modelling

We present here the 1D forward modelling, which takes the four electromagnetic properties into account (see also Ward and Homann 1988). It allows us to define the apparent properties when the ground is assumed to be homogeneous, and to inverse for properties and thicknesses of the successive layers when a multi-layer model is considered.

- For horizontal coplanar (HCP), where the transmitter is a vertical magnetic dipole, M_z, located at (*0, 0, -h*) and the receiver a small coil located at *(0, L, -h)*,

$$H_z = \frac{M_z}{4\pi}\int_0^\infty \lambda^2 R_v(\lambda) e^{-2u_0 h} J_0(\lambda L) d\lambda \qquad (1)$$

- For vertical coplanar (VCP), where the transmitter is a horizontal magnetic dipole, Mx, located at *(0, 0, -h)* and the receiver a small coil located at *(0, L, -h)*,

$$H_x = \frac{M_x}{4\pi}\left\{-\gamma_0^2\int_0^\infty R_H(\lambda) e^{-2u_0 h} J_0(\lambda L) d\lambda + \frac{1}{L}\int_0^\infty \frac{R_1(\lambda) e^{-2u_0 h}}{\lambda} J_1(\lambda L) d\lambda\right\} \qquad (2)$$

In these expressions J_0 and J_1 are the Bessel's function of the first kind, $u_0 = \sqrt{\lambda^2 + \gamma_0^2}$ with $\gamma_0^2 = -\varepsilon_0 \mu_0 \omega^2$, and $R_v(\lambda) = \frac{\lambda}{u_0}\frac{\frac{u_0}{\mu_0} + Y_1}{\frac{u_0}{\mu_0} - Y_1}$, Y_1 being recursively calculated by starting at the top of the deepest layer, N, by $Y_N = -\frac{u_N}{\mu_N}$ and using the formula: $Y_i = \frac{u_i}{\mu_i}\frac{Y_{i+1} - \frac{u_i}{\mu_i}\tanh u_i e_i}{\frac{u_i}{\mu_i} - Y_{i+1}\tanh u_i e_i}$. In this formula, e_i is the thickness of the ith layer, and $u_i = \sqrt{\lambda^2 + \gamma_i^2}$ with $\gamma_i^2 = i\sigma_i \mu_i \omega - \varepsilon_i \mu_i \omega^2$ and $i = \sqrt{-1}$.

$R_1(\lambda) = \gamma_0^2 R_H(\lambda) + u_0^2 R_v(\lambda)$. The function $R_H(\lambda)$ is calculated by $R_H(\lambda) = \frac{\lambda}{u_0} \frac{\frac{u_0}{i\omega\varepsilon_0} + Z_1}{\frac{u_0}{i\omega\varepsilon_0} - Z_1}$, Z_1 being recursively calculated by starting at the top of the deepest layer by $Z_N = -\frac{u_N}{\sigma_N + i\omega\varepsilon_N}$ and using the formula: $Z_i = \frac{u_i}{\sigma_i + i\omega\varepsilon_i} \frac{Z_{i+1} - \frac{u_i}{\sigma_i + i\omega\varepsilon_i} \tanh u_i e_i}{\frac{u_i}{\sigma_i + i\omega\varepsilon_i} - Z_{i+1} \tanh u_i e_i}$. To get results which are independent of the transmitted power, the secondary field expressions are usually normalized by the primary amplitude, $H_p = M/(4\pi L^3)$ and the measurements are expressed in terms of H_s/H_p, in ppm (parts per million) or in ppt (parts per thousand) depending on the device manufacturer (ppm for the EMP400 and ppt for the EM31, 1ppt=1000 ppm).

To illustrate the physical meaning of these complex analytic expressions by showing the influence of any property or instrument parameter, approximations (Thiesson et al. 2014) can be calculated based on the range of values of the different properties. The static approximation ($\omega \to 0$) establishes that the ratio of the secondary field to the primary field for a coplanar instrument (HCP or VCP) located at h=0 clearance above the surface would be $\frac{H_s}{H_p} \cong -\frac{\kappa_{ph} - i\kappa_{qu}}{2}$. This suggests that the magnetic susceptibility response would be in-phase, the viscosity response in quadrature and their dependence on frequency and coil separation limited. Furthermore, the Low Induction Number (LIN) approximation, $\sigma\mu\omega L^2 << 1$, which corresponds, if $\mu = \mu_0$ and h=0, to $\frac{H_s}{H_p} \cong -\frac{i\sigma\mu_0\omega L^2}{4}$ suggests that the conductivity effects would mainly be in quadrature and proportional to the conductivity, the frequency and the square of the coil separation (this approximation is the one commonly used by most instrument manufacturers to define ECa).

If we take into account the permittivity, this last approximation becomes $\frac{H_s}{H_p} \cong -\frac{i\sigma\mu_0\omega L^2}{4} + \frac{\varepsilon_0\varepsilon_r\mu_0\omega^2 L^2}{4}$, which suggests that the permittivity response would be first order in-phase and would drastically increase with the frequency and coil separation. Consequently, the in-phase response can be dependent on both the magnetic susceptibility and the relative permittivity. Note also that even if the displacement currents are negligible in comparison with conduction ones, $|\sigma| >> |i\varepsilon_0\varepsilon_r\omega|$, the permittivity response may be significant in comparison with the susceptibility response.

2-4. *Instrument calibration and sensitivity analysis*

At each geometrical configuration and frequency an instrument measures two quantities, the in-phase and quadrature responses, and it is important to understand the influence of each of the four properties (electrical conductivity (or Eca), dielectric permittivity, magnetic susceptibility (or Msa) and magnetic viscosity) on these responses.

To assess this, the calculated responses, as a function of each of the four properties, are expressed by the ratios of the secondary field to the secondary field of a reference ground, where σ=0.01 Sm^{-1}, ε_r=200, κ_{ph}=100 10^{-5} SI and κ_{qu} =0.06κ_{ph}. In this trial each property is varied from 0.1 to 10 times that of the value used in the reference case value. Figure 3 presents the in-phase modelled responses for the EMP400, and Figure 4 those for the quadrature situation for both configurations and each frequency. For the low-frequency instrument, the influence of permittivity is negligible, as illustrated by the flat curve in Figure 3 at all configurations and frequencies. The magnetic susceptibility dominates the in-phase response with a linear dependence (Fig. 3), and conductivity controls the quadrature responses with a quasi-linear dependence (Fig. 4). These characteristics are in complete agreement with all that has already been published (McNeill 1980, Tabbagh 1986a). However, a precise interpretation needs to

take the effect of the conductivity on the in-phase response into consideration, which increases, but not in direct proportion to the conductivity (Fig. 3), and the effect of the magnetic viscosity on the quadrature response (Fig. 4). The procedure to determine these properties is presented in Simon et al. (2015).

No drift has been observed for the EMP400 (but the temperature changes during the acquisition remained limited). A major drawback of the raw data sets is that they first require the determination of the zero offsets or signal shifts. For in-phase components such shifts are mainly caused by mechanical deformations that modify the direct influence of the primary field, but, surprisingly, offsets also exist in quadrature. For each configuration, this step was achieved by a trial and error process to overcome this problem. In quadrature, the different apparent conductivity values, calculated at each frequency and by considering the differences between each frequency pair, must be as close as possible to each other and positive, while the magnetic viscosity must be positive (Simon et al. 2015). In-phase, the different susceptibility values must be as close as possible and positive. The zero offsets are given in Table 1.

Following the same approach as for the EMP400, Figures 5 and 6 show the evolution of the ratio of the in-phase and quadrature secondary fields to those of the reference case for the EM31, in which each property varies from 0.1 to 10 times the value used in the reference case. The dependence of the quadrature response on magnetic viscosity is, in this case (h=1m), quasi null (Fig. 6); therefore, the conductivity determination can be directly achieved with this component at a single frequency. The in-phase component is sensitive to conductivity, permittivity and in-phase magnetic susceptibility (Fig. 5), the permittivity response is illustrated by a quasi-flat curve for all configurations and clearance; it is significantly smaller than those of the susceptibility and conductivity. Determination of the apparent properties thus follows a two-step approach: (1) determination of the apparent conductivity using the quadrature response; (2) taking into account the in-phase electrical conductivity response, determination either of the

apparent magnetic susceptibility or of both the permittivity and the susceptibility if both HCP and VCP configurations are available. This last step follows the linear process described in Benech et al. (2016).

With EM31, no zero offset correction is necessary for the quadrature part of the signal because of the good field calibration of the device achieved by the manufacturer and of the large coil spacing which increases the signal/noise ratio. On the other hand, the zero offset corrections for the in-phase part of the signal must be evaluated (this component is used in metal detection). Here, following the same the calibration protocol as for the EMP400, in-phase signal offsets were established at 56 ppt for HCP (56000 ppm) and 64 ppt (64000 ppm) for VCP by a trial and error process. These high values correspond to a significant uncertainty regarding the exact offset value, but not for the spatial variations of the properties.

3- Results

3-1. *Apparent property maps*

Each apparent property is defined here as the property of homogeneous flat ground that would give the same response as that obtained with the considered instrument.

The maps resulting from the EMP400 measurements are presented in Figure 7 for the apparent conductivity, and in Figure 8 for the apparent magnetic susceptibility. As the magnetic viscosity, the conductivity and the depth of investigation are independent of the frequency, the difference in quadrature responses between the 15 kHz and 5 kHz frequencies allowed us to remove the magnetic viscosity effect (Simon et al. 2015). To determine the electrical conductivity we thus compared these differences to the corresponding theoretical reference curves calculated from equations (1) for HCP, or (2) for VCP. We also used theoretical reference curves for each frequency to determine the electrical conductivity using the

quadrature responses. Using this electrical conductivity value, it is then possible to extract the magnetic viscosity value, which is shown for the VCP and HCP configurations in Figure 9.

As illustrated in Figure 7, the maps of electrical conductivity at the different frequencies show identical results, in complete agreement with the values of the Induction Number that establish the similarity in depths of investigation. This result corroborates the solution adopted for the computation of magnetic viscosity. The HCP and VCP maps for apparent conductivity are also very similar. The HCP configuration exhibits a greater range of values, and lower values at the edge of the depression, in agreement with an investigation at greater depth. In the center, the values are higher than 0.04 $S.m^{-1}$ and, as expected, confirm the clayey nature of the filling and clearly delineate the topographic trough.

For magnetic properties, reference curves deduced from equations (1) and (2) are used to determine the apparent magnetic susceptibility, taking into account the estimated electrical conductivity at each point. The HCP and VCP susceptibilities are globally very high, between 300 and 3,800 10^{-5} SI, in agreement with the presence of a basaltic rock substratum (Trigui and Tabbagh 1990). The differences between results for the three frequencies are small, as predicted by the theory. The strong similarity confirms the efficiency of the correction of the induction effect on the in-phase signal for HCP and VCP configurations, respectively. However, the sediment in-fill has lower susceptibility values than the border, at around 700 10^{-5} SI. The horizontal delineation is in complete agreement with that of the conductivity. The magnetic viscosity is relatively low and its lateral distribution differs from that of the susceptibility. In HCP the magnetic viscosity (depth of investigation of 0.2 L) is higher than in VCP (depth of investigation: 0.6 L) which suggests that it is stronger for the superficial layer of the depression. This observation is in complete agreement with the field observations. The uppermost 45-50 centimeters, of slightly varying thickness, contain many sherds and are very different to the deeper layer (Mayoral et al. 2018a). The ratio $\frac{\kappa_{qu}}{\kappa_{ph}}$ values, being higher than 4% inside the

topographic trough and lower than 1% at the border, confirm that the basalt mainly contains stable single-domain magnetic grains (high susceptibility and low magnetic viscosity) while the in-fill has been enriched by pedogenic processes - such as redoximorphic processes or alteration of mineral grains (Mayoral et al. 2018) - into smaller single-domain grains closer in volume to the superparamagnetic range (Maher and Taylor 1988). By comparison, a ratio of 6% or more is expected for common non-hydromorphic soils (Dabas and Skinner 1993). As only a single frequency device (MS2-E) was used on the laboratory soil sample measurements, no direct comparison in terms of frequency variation for the susceptibility can be carried out for this field observation.

HCP and VCP conductivity maps obtained from the EM31 quadrature signal (Figure 10) confirm the horizontal distribution shown by the EMP400 maps. As expected, given that the investigation depth is greater, the conductivity values are about one and a half times lower than for the EMP400.

For the in-phase signal, due to the longer coil separation, the effects of both the magnetic susceptibility and the relative permittivity should be considered. The raw data variability is presented in Table 2. The sensitivities of EM31 to the homogeneous ground properties are given in Table 3. The lower sensitivity to κ_{ph} of the HCP response is due to the instrument's clearance, h=1 m, because this elevation is close to the change in sign which occurs in the HCP configuration for magnetic responses (at h=1.39 m for a coil separation of 3.66 m). If we calculate the apparent magnetic susceptibility from the in-phase responses without considering the relative permittivity, the discrepancy between HCP and VCP results is marked (Figure 11): the spatial distributions are significantly different with a higher dynamic in HCP (in the range 7,500 to 50,000 10^{-5} SI), and a lower dynamic in VCP (in the range 2,500 to 18,000 10^{-5} SI). As potentially imperfect offset corrections would increase this effect, the significant difference

between the two configurations can probably be explained by the sensitivity to susceptibility distribution in relation to the depth.

The maps presented in Figure 12 show the results with both the permittivity and the susceptibility taken into account to define the homogeneous half-space properties using both HCP and VCP in-phase values (Benech et al. 2016). In these apparent property maps, the susceptibility variations remain similar to those observed in Figure 11, whereas the permittivity variations are huge, with a 140,000 interquartile deviation and a big gap for the zero offset. The range of values looks unlikely and it can only be assumed that the basalt border has lower values than the sedimentary in-fill in the depression. The high susceptibility values agree with the presence of a basaltic substratum underlying the sedimentary in-fill and are logically greater than the values delivered by the EMP400. The permittivity values logically result from the low sensitivity presented in Table 3. Considering the high magnetic context and the unlikely apparent permittivity values, the intervention of a permittivity response looks unrealistic. This conclusion will be reconsidered later on when considering a layered terrain.

From the apparent property mapping, it can be seen that the filling is more conductive and possibly more polarizable than the surrounding basalt. Its conductivity indicates that it is dominated by fine particles. It has a lower magnetic susceptibility with respect to the surrounding weathered basalt, but a higher magnetic viscosity. Taking all this into account, the electromagnetic properties can provide an accurate description of magnetic behavior in addition to the electrical properties. We are then able to describe not only the clay filling of the depression but also some pedogenetic phenomena, and even provide further details about the lateral and horizontal variations in the hydromorphic soils in a volcanic context, which is poorly revealed by a single electrical conductivity mapping based approach.

3-2 *1D inversion processing using quadrature data*

Based on the 1D forward modelling (Guérin et al. 1996), we carried out 1D inversions, firstly considering the electrical conductivity alone, then taking all the electromagnetic properties of the soil into account. Due to the quality of the data, it was not necessary to select a lateral smoothing inversion process, as it was possible to achieve this point by point. The forward operator, $\boldsymbol{G}$, uses equation (1) for HCP data, and equation (2) for VCP data. At each point, an iterative damped least square linearization was applied, which started from the $\boldsymbol{m_0}$ vector of the *a priori* values of the conductivity and/or thickness and calculated $\boldsymbol{\Delta m}$, the solution of the equation, $(J^T J + \lambda I)\Delta m = J^T (d - Gm_{i-1})$, $\boldsymbol{m_{i-1}}$ being the vector solution at the (i-1)th iteration, $\boldsymbol{d}$ the vector of the data, $\boldsymbol{I}$ the identity matrix, $\boldsymbol{J}$ the Jacobian of $\boldsymbol{G}$, and λ the regularization parameter. λ has a starting value equal to half of the trace of the $\boldsymbol{J^T J}$ matrix.

To carry out a more in depth characterization of the sedimentary in-fill, we attempted to reconstruct the depth to the bedrock using a 1D inversion in a two-step approach. In the first step, we only considered the HCP and VCP quadrature responses by using the differences between 15 kHz and 5 kHz for the EMP400 quadrature data, and the quadrature data at 9.8 kHz for the EM31. In the second step, we considered the four properties using eight independent sets of data: quadrature and in-phase. For the conductivity profile, following comparison with the field data (Mayoral et al. 2018), we used a three-layer model (see Figure 2) with a superficial soil layer (the two top clay loam layers), a second layer corresponding to the sedimentary in-fill (massive heavy clay layer), and a third layer corresponding to the possibly weathered basaltic rocks (sandy bottom and weathered basaltic rock layers). As an initial model of the parameters, the superficial layer had a conductivity of σ_1=20 mS.m^{-1} (or 50 Ω.m resistivity) and a thickness of e_1=0.15 m; the sedimentary in-fill a conductivity of σ_2=83.3 mS.m^{-1} (or 12 Ω.m resistivity) (a little bit higher than the EMP400 minimum) and a thickness of e_2=1 m; and the basement a conductivity of σ_3=3.33 mS.m^{-1} (or 300 Ω.m resistivity) (lower than any of the EM31 HCP measurements). The conductivities and thicknesses of the different layers were

tested and it was observed that the parameters of the uppermost layer had only a very limited influence. EMI inversions were also subject to so-called 'cases of equivalence': in the case of a conducting layer between two more resistive ones (H type for vertical electrical soundings), the conductive layer can be exchanged for any other layer with the same $\frac{e^{\frac{2}{3}}}{\rho}$ ratio (Guérin et al. 1996). Finally, by allowing only e_2 and σ_1 to vary, and keeping the other parameters fixed, the thickness distribution presented in Figure 13 was obtained.

These results suggest that the 0.75 m thickness value corresponds to the contour of the depression itself, due to a thickness contrast with the surrounding second layer. This thickness variation is in complete agreement with the profile published by Guillemoteau (2016) when interpreting DualEM421 results and with the field observation (Mayoral et al. 2018). We also carried out a control of the inversion results by comparing field observations with the results of the inversion using the quadrature part of the signal. Figure 14(a) shows that the estimations of the thicknesses of the three layers made it possible to clearly describe the depth of the high clay content layers filling the depression. Only one of the logs (log 3) located in the central trench of the site (Figure 14), does not fit the inversion results. This difference could derive from the 1D interpretation which leads to a smoothed model of the bottom of the second layer where there is in reality a local rise in the basalt.

3-3 *1D inversion using both quadrature and in-phase data sets*

Using the three-layer model obtained by 1D modelling of the conductivity results, the other EM properties for each layer were determined point by point. The same issue as above recurs: is it possible to determine both the susceptibility and permittivity or can the influence of the permittivity be neglected? In other words, which hypothesis gives the more realistic

results with respect to the geological/pedological context and the external information available describing the depression as having an irregular base shaped into several alteration zones?

When the permittivity is neglected, the magnetic susceptibility obtained for the second layer by using four sets of in-phase data is presented in Figure 15. The permittivity for the three layers is fixed at an ordinary value of: $\varepsilon_{r1}=\varepsilon_{r2}=\varepsilon_{r3}=200$, and with $\kappa_{ph1}=500\ 10^{-5}$ SI and $\kappa_{ph3}=2000\ 10^{-5}$ SI. The map is in agreement with the apparent susceptibility maps in terms of the lateral distribution and the parameter's magnitude (Figures 8 and 11).

Figure 16 presents the results for the case where the permittivity of the second layer is variable. These results are obtained with $\varepsilon_{r1}=\varepsilon_{r3}=2000$ but are practically independent of the first and third layer fixed permittivity values. The susceptibility is reduced by a factor close to two and, again, the permittivity values are very high and unrealistic. For a permittivity of 10^6 (median value obtained), the quantity $\omega\varepsilon_r\varepsilon_0$ would equal 0.54 Sm^{-1}, seven times greater than the conductivity itself (83 $mS.m^{-1}$). Considering this extremely high and unlikely estimated range of values of dielectric permittivity, the second hypothesis, where the variations of the permittivity are not characterized for the EMP400 and EM31 instruments, and where the in-phase results correspond to magnetic susceptibility only, must be adopted.

A comparison with the susceptibility observed at a scale of 1 cm in the cores ('U-Channel' cores), which is summarized in Figure 14, shows a significant discrepancy between the magnitude of inverted in-field susceptibility values and the laboratory ones (MS2-E) for the in-fill of the depression. This discrepancy is explained if one considers that the presence of basalt gravels and pebbles (with around 12000 10^{-5} SI susceptibility) is taken into account by in-field measurements rather than laboratory one on the cores. These coarse particles would correspond to one fourth or one fifth of the sediment volume at a metric scale.

4 Conclusion

This case study confirms the relevance of this type of light EMI apparatus for the rapid exploration of superficial sedimentary/pedological formations, and will increase the reliability of future sediment sampling at the Lac du Puy. Two different single receiver instruments were used, although a multi-receiver/multi-frequency apparatus would produce the same results and be easier to use.

The highly magnetic context due to the basaltic substrate led us to look at the in-phase measurements and try to describe the magnetic susceptibility and magnetic viscosity of the in-fill. This process is more common for shorter separation instruments, but nothing has yet been published about this usage for the EM31. The superficial soil and the depression in-fill have a lower magnetic susceptibility and a higher magnetic viscosity than the surrounding weathered basalt and their spatial distribution is slightly different to that of the sediment thickness. Due to the improbable magnitude of the inverted permittivity results, no role can be attributed to the dielectric permittivity variations and the full signal can be attributed to the complex magnetic susceptibility and electrical conductivity. Further studies should be done in the future to assess the effect of permittivity on the in-phase EM31 signal. In this volcanic substrate case study, magnetic susceptibility responses outweigh the electrical polarization when using the EM31. It would be worth doing further investigations in order to assess the potential for this type of instrument in other environments, such as coastal areas or salt-rich soils.

In conjunction with the field characterization of the sedimentary accumulation, measurements of the quadrature and in-phase components of the Hs/Hp ratio using the HCP and VCP configurations for both instruments provided a clear description of the conductivity variations. It enabled the Lac du Puy sedimentary in-fill to be identified, by mapping the shape and morphology of the bedrock, lending support to the hypothesis that the depression is a pseudo-sinkhole (Mayoral et al 2018a).

The analysis of a combination of magnetic properties allowed the 3D morphology of the sedimentary in-fill to be determined across the basin, and provided stratigraphic and sedimentological information. In addition, selected magnetic properties provided information on the spatial variation of some key features related to hydromorphic processes, in particular clayey granularity and the development of iron oxides/hydroxides. These findings, which will be further tested and refined in other parental rocks, could provide new means of rapid spatial and pedological characterization of hydromorphic soils and palaeosoils, with useful applications for palaeoenvironmental studies.

References

Benech C., Lombard P., Réjiba F., Tabbagh A., 2016. Demonstrating the contribution of dielectric permittivity to the in-phase EMI response of soils: example of an archaeological site in Bahrain. Near Surface Geophysics, 14-4, 337-344.

Bendjoudi H., Weng P., Guérin R., Pastre J. F., 2002. Riparian wetlands of the middle reach of the Seine river (France): historical development, investigation and present hydrologic functioning, a case study. Journal of Hydrology, 263, 131-155.

Boaga J., 2017. The use of FDEM in hydrogeophysics: A review. Journal of Applied Geophysics, 139, 36-46.

Cuenca Garcia C., 2019. Soil geochemical methods in archaeo-geophysics: Exploring a combined approach at sites in Scotland, Archaeological Prospection, 26,1, 57-72.

Dabas M., Skinner J., 1993. Time domain magnetization of soils (VRM), experimental relationship to quadrature susceptibility. Geophysics, 58, 326-333.

de Jong E., Ballantyne A. K., Cameron D. R., Read D. W. L., 1979. Measurement of Apparent Electrical Conductivity of Soils by an Electromagnetic Induction Probe to Aid Salinity Surveys. Soil Science Society of America Journal, 43-4, 810-812.

De Smedt P., Saey T., Meerschman E., De Reu J., De Clercq W., Van Meirvenne M., 2014. Comparing apparent magnetic susceptiblity measurements of a multi-receiver EMI sensor with topsoil and profile magnetic susceptibility data over weak magnetic anomalies, Archaeological prospection, 21, 2, 103-112

Doolittle J. A., Brevik E. C., 2014. The use of electromagnetic induction techniques in soils studies. Geoderma, 223-225, 33-45.

Dotterweich M., 2008. The history of soil erosion and fluvial deposits in small catchments of central Europe: Deciphering the long-term interaction between humans and the environment — A review. Geomorphology, 101, 192–208.

Dreibrodt S., Lomax J., Nelle O., Lubos C., Fischer P., Mitusov A., Reiss S., Radtke U., Nadeau M., Grootes P. M., & Bork H.-R., 2010. Are mid-latitude slopes sensitive to climatic oscillations? Implications from an Early Holocene sequence of slope deposits and buried soils from eastern Germany. Geomorphology, 122, 351–369.

Frischknecht F. C., Labson V. F., Spies B. R., Anderson W. L., 1991. Profiling Methods Using Small Sources. In Electromagnetic Methods in Applied Geophysics: Volume 2, Application, Parts A and B, M. N. Nabighian ed., SEG, pp105-270.

Grison H., Petrovsky E., Stejskalova S., Kapicka A., 2015. Magnetic and geochemical characterization of Andosols developed on basalts in the Massif Central, France, Geochemistry, Geophysics, Geosystems, 16, 1348–1363, doi:10.1002/2015GC005716.

Guérin R., Méhéni Y., Rakotondrasoa G., Tabbagh A., 1996. Interpretation of Slingram conductivity mapping in near-surface geophysics: using a single parameter fitting with 1D model. Geophysical Prospecting, 44, 233-249.

503 Greffier G., Restituito J., & Héraud H., 1980. Aspects géomorphologiques et stabilité des
504 versants au sud de Clermont-Ferrand. Bulletin de liaison du Laboratoire des Ponts et
505 Chaussées, 107, 17–26.
506 Guillemoteau J., Simon F.-X., Lück E., Tronicke J., 2016. 1D sequential inversion of portable
507 multi-configuration electromagnetic induction data. Near Surface Geophysics, 14, 411-
508 420.Henkner J., Ahlrichs J. J., Downey S., Fuchs M., James B. R., Knopf T., Scholten T.,
509 Teuber S., Kühn P., 2017. Archaeopedology and chronostratigraphy of colluvial deposits as a
510 proxy for regional land use history (Baar, southwest Germany). Catena, 155, 93–113.
511 Hendrickx J.M. H., Borchers B., Corwin D. L., Lesch S. M., Hilgendorf A. C., Schlue J., 2002.
512 Inversion of Soil Conductivity Profiles from Electromagnetic Induction Measurements:
513 Theory and Experimental Verification. Soil Science Society of America Journal, 66, 673-685.
514 Jordanova, N. 2017. Soil Magnetism. Applications in Pedology, Environmental Science and
515 Agriculture, London, UK, Academic Press.
516 Maher B. A., Taylor R. M., 1988. Formation of ultrafine-grained magnetite in soils. Nature 336,
517 368-370.
518 Mayoral A., Peiry J.L., Berger J.F., Ledger P.M., Depreux B., Simon F.X., Milcent P.Y., Poux
519 M., Vautier F., Miras Y., 2018a. Geoarchaeology and chronostratigraphy of the Lac du Puy
520 intraurban protohistoric wetland, Corent, France, Geoarchaeology, 33, 5, 594-604
521 Mayoral A., Peiry J.L., Berger J.F., Simon F.X., Vautier F., Miras Y., 2018b. Origin and
522 Holocene geomorphological evolution of the landslide-dammed basin of la Narse de la Sauvetat
523 (Massif Central, France) Geomorphology, 320, 162-167
524 McNeill J.D. 1980. Electromagnetic terrain conductivity measurement at low induction
525 numbers. Geonics Limited Technical Note TN–6, 15p.
526 McNeill J. D., 2013. The magnetic susceptibility of soils is definitely complex. Geonics Limited
527 Technical Note TN-36, 28p.

Nehlig P., Boivin P., De Goër A., Mergoil J., Sustrac G., Thiéblemont D., 2003. Les volcans du Massif central. Géologues (sp. issue), 1–41.

Neely H. L., Morgana C. L. S., Hallmark C. T., McInnes K. J., Molling C. C., 2016. Apparent electrical conductivity response to spatially variable vertisol properties. Geoderma, 263, 168–175.

Saey T., Simpson D., Vitharana U. W. A., Vermeersch H., Vermang J., Van Meirvenne M., 2008. Reconstructing the paleotopography beneath the loess cover with the aid of an electromagnetic induction sensor. Catena, 74, 58-64.

Scollar I., Tabbagh A., Hesse A., Herzog I., 1990. Archaeological prospecting and remote sensing. Cambridge University Press, 674p.

Simon F.–X., Sarris A., Thiesson J., Tabbagh A., 2015. Mapping of quadrature magnetic susceptibility/magnetic viscosity of soils by using multi-frequency EMI. Journal of Applied Geophysics, 120, 36-47.

Simon F.-X., Tabbagh A., Donati J., Sarris A., 2019. Permittivity mapping in the VLF-LF range using a multi-frequency EMI device: first tests in archaeological prospection, Near Surface Geophysics,

Sudduth K. A., Kitchena N. R., Wieboldb W. J., Batchelorc W. D., Bollerod G. A., Bullockd D. G., Claye D. E., Palmb H. L., Piercef F. J., Schulerg R. T., Thelenh K. D., 2005. Relating apparent electrical conductivity to soil properties across the north-central USA. Computers and Electronics in Agriculture 46, 263–283.

Tabbagh A., 1986a. Applications and advantages of the Slingram electromagnetic method for archaeological prospecting. Geophysics, 51-3, 576-584.

Tabbagh A., 1986b. What is the best coil orientation in the Slingram electromagnetic prospecting method? Archaeometry, 28-2, 185-196.

552 Thiesson J., Kessouri P., Schamper C., Tabbagh A. 2014. Calibration of frequency-domain
553 electromagnetic devices used in near-surface surveying. Near Surface Geophysics, 12, 481-491.
554 Tite M. S., Mullins C. E. 1970. Electromagnetic prospecting on archaeological sites using a soil
555 conductivity meter. Archaeometry, 12, 97-104.
556 Triantafilis J., Monteiro Santos F. A., 2010. Resolving the spatial distribution of the true
557 electrical conductivity with depth using EM38 and EM31 signal data and a laterally constrained
558 inversion model. Australian Journal of Soil Research, 48, 434–446.
559 Triantafilis, J., Terhune IV, C.H., Monteiro Santos F.A., 2013a. An inversion approach to
560 generate electromagnetic conductivity images from signal data. Environmental Modelling and
561 Software, 43,88-95.
562 Triantafilis J., Monterio Santos, F.A., 2013b. Electromagnetic conductivity imaging (EMCI) of
563 soil using a DUALEM-421 and inversion modelling software (EM4Soil). Geoderma, 211-212
564 Trigui M., Tabbagh A., 1990. Magnetic susceptibilities of oceanic basalts in alternative fields.
565 Journal of Geomagnetism and Geoelectricity, 42, 621-636.
566 Ward S. H., Homann G. W., 1988. Electromagnetic Methods in Applied Geophysics: Volume
567 1, Theory, M. N. Nabighian ed., SEG Publications, Tulsa OK.
568
569
570 **Figure captions**
571 Figure 1: Schematic view of the relationship between the soil properties, the geophysical
572 properties and the resulting dataset process during 1D inversions.
573 Figure 2: a) Site location in Central France, b) Aerial view of the Plateau de Corent and the Lac
574 du Puy area, c) Ortho-photography of the depression with cross-section location marked,
575 d) Cross-section showing the main sedimentary units and their respective average
576 magnetic susceptibility measurements (MS2-E, Bartington Ldt, device).

Figure 3: EMP400 (L=1.21 m, h=0.25 m) ratio of the in-phase secondary field to the in-phase secondary field of the reference model for relative permittivity (a), magnetic susceptibility (b) and electrical conductivity (c), for the three frequencies used (5 kHz in red, 8 kHz in green and 15 kHz in blue), for HCP (solid lines) and VCP (dashed lines) configurations.

Figure 4: EMP400 (L=1.21 m, h=0.25 m) ratio of the quadrature secondary field to the quadrature secondary field of the reference model for magnetic viscosity (a), and electrical conductivity (b), for the three frequencies used (5 kHz in red, 8 kHz in green and 15 kHz in blue), for HCP (solid lines) and VCP (dashed lines) configurations.

Figure 5: EM31 (L=3.66 m, f=9.8 kHz) ratio of the in-phase secondary field to the in-phase secondary field of the reference model for relative permittivity (a), magnetic susceptibility (b) and electrical conductivity (c), for HCP (solid lines) and VCP (dashed lines) configurations at h=1 m (in red) and h=0.3 m (in blue) clearances.

Figure 6: EM31 (L=3.66 m, f=9.8 kHz) ratio of the quadrature secondary field to the quadrature secondary field of the reference model for magnetic viscosity (a) and electrical conductivity (b), for HCP (solid line) and VCP (dashed line) configurations at h=1 m (in red) and h=0.3 m (in blue) clearances.

Figure 7: EMP400 apparent conductivity maps: determined using the difference in quadrature response between 15 kHz and 5 kHz (Simon et al. 2015) (above), and at each frequency (5, 8 and 15 kHz) (below).

Figure 8: EMP400 apparent magnetic susceptibility maps, κ_{ph}, at the three frequencies used (5, 8 and 15 kHz), for HCP (left) and VCP (right) configurations.

Figure 9: EMP400 apparent magnetic viscosity map κ_{qu} for HCP (left) and VCP (right) configurations.

Figure 10: EM31 apparent electrical conductivity maps for HCP (left) and VCP (right) configurations.

602 Figure 11: EM31 apparent magnetic susceptibility, κ_{ph}, maps determined without taking the
603 relative permittivity, ε_r, response into account for the HCP and VCP configurations.
604 Figure 12: EM31 maps of the apparent magnetic susceptibility, κ_{ph}, and of the apparent relative
605 permittivity, ε_r, deduced from both in-phase HCP and VCP responses.
606 Figure 13: Thickness of the second layer, e_2, resulting from a 1D inversion when σ_1 and e_2 are
607 variable: a) thickness map of e_2, b) oblique view of the 3D representation of e_2.
608 Figure 14: a) comparison of field observations and results based on the estimation of the
609 thickness of each layer for the 3-layer model, b) location of the trench and log observation,
610 c) Value of the magnetic susceptibility measurement of the MS2-E (Bartington Ltd)
611 carried out on a 'U-channel' core from log 3.
612 Figure 15: Inversion of the magnetic susceptibility of the second layer, ignoring permittivity
613 variations.
614 Figure 16: Inversion of both the magnetic susceptibility and the dielectric permittivity of the
615 second layer.
616
617
618 **Tables :**
619 Table 1: EMP400 zero offset corrections in ppm
620 Table 2: Variabilities of the in-phase raw data from EM31
621 Table 3: Sensitivities of the EM31 in-phase responses to homogeneous ground susceptibility
622 and permittivity when h=1 m
623
624
625

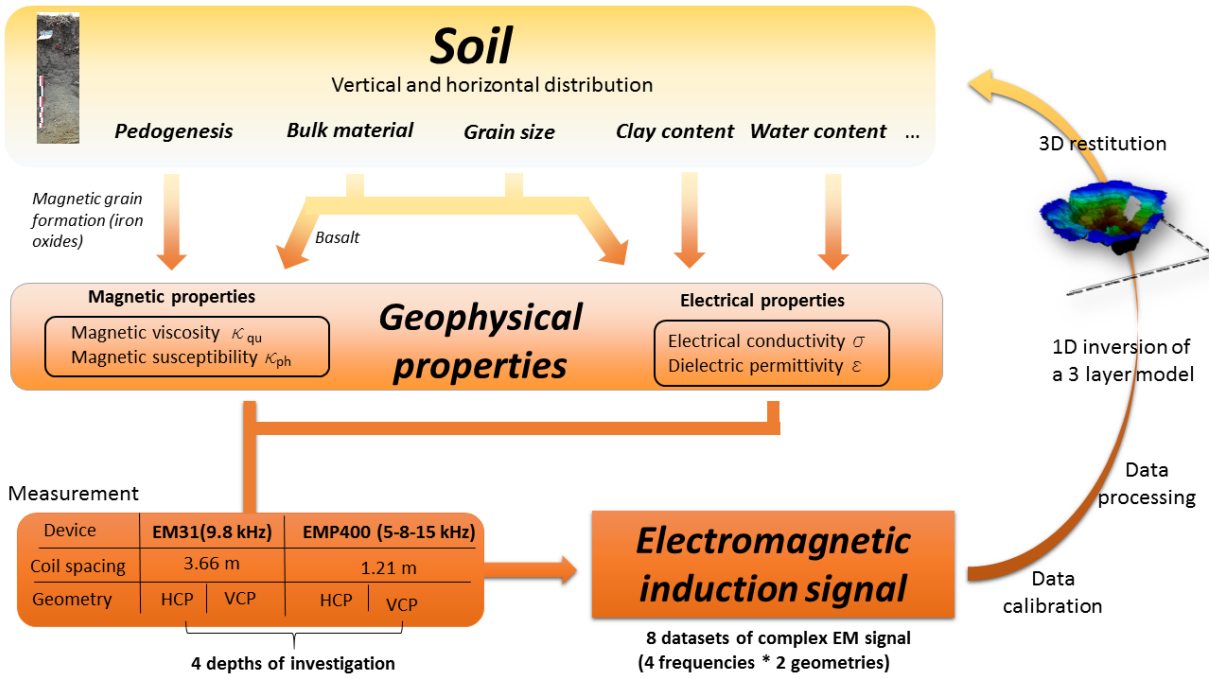

626

627 Figure 1: Schematic view of the relationship between the soil properties, the geophysical

628 properties and the resulting dataset process during 1D inversions.

629

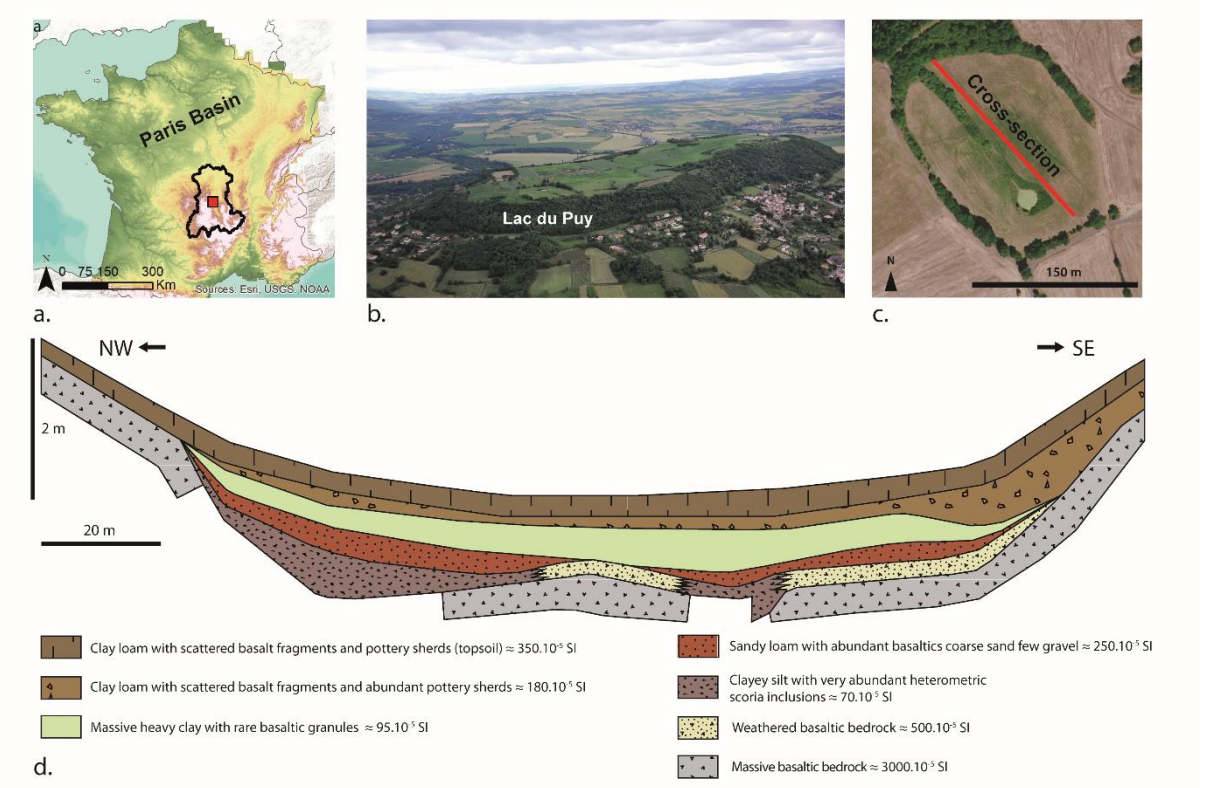

Figure 2: a) Site location in Central France, b) Aerial view of the Plateau de Corent and the Lac du Puy area, c) Ortho-photography of the depression with cross-section location marked, d) Cross-section showing the main sedimentary units and their respective average magnetic susceptibility measurements (MS2-E, Bartington Ldt, device).

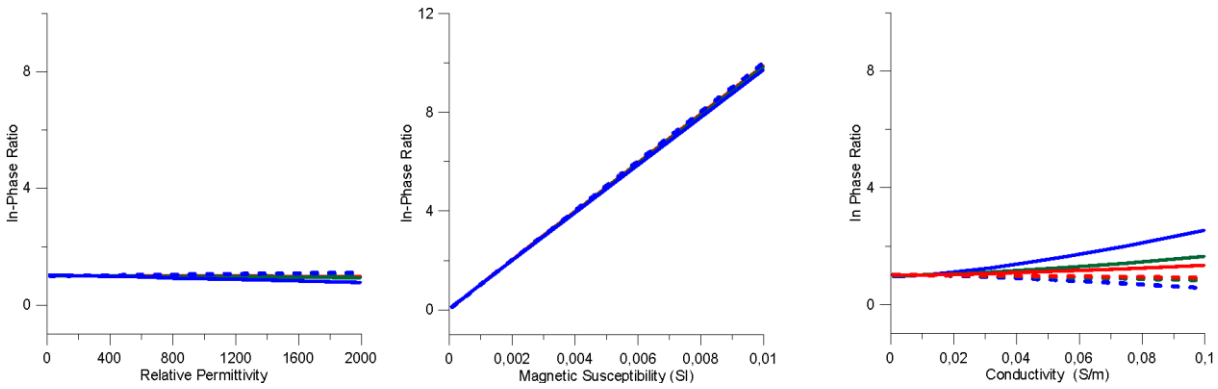

Figure 3: EMP400 (L=1.21 m, h=0.25 m) ratio of the in-phase secondary field to the in-phase secondary field of the reference model for relative permittivity (a), magnetic susceptibility (b) and electrical conductivity (c), for the three frequencies used (5 kHz in red, 8 kHz in green and 15 kHz in blue), for HCP (solid lines) and VCP (dashed lines) configurations.

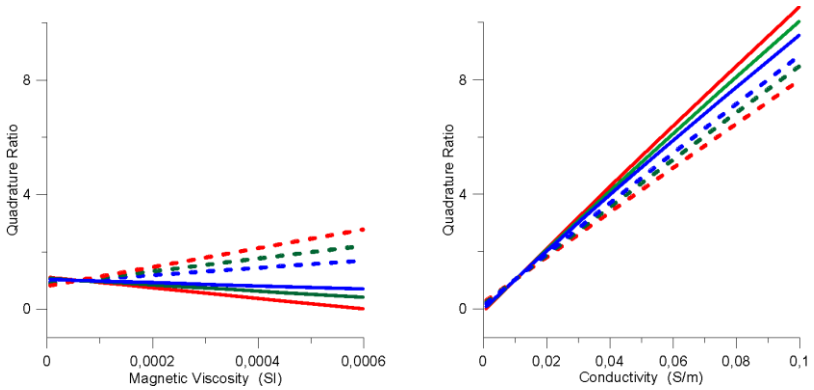

Figure 4: EMP400 (L=1.21 m, h=0.25 m) ratio of the quadrature secondary field to the quadrature secondary field of the reference model for magnetic viscosity (a), and electrical conductivity (b), for the three frequencies used (5 kHz in red, 8 kHz in green and 15 kHz in blue), for HCP (solid lines) and VCP (dashed lines) configurations.

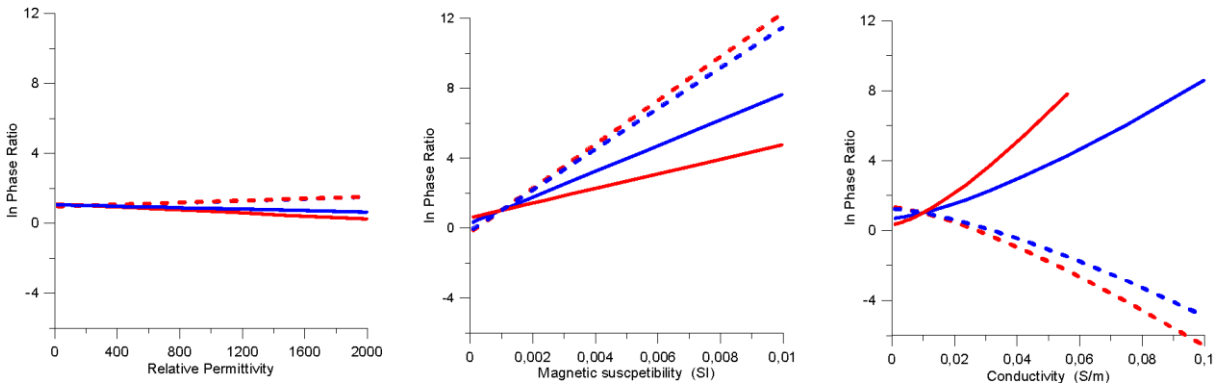

Figure 5: EM31 (L=3.66 m, f=9.8 kHz) ratio of the in-phase secondary field to the in-phase secondary field of the reference model for relative permittivity (a), magnetic susceptibility (b) and electrical conductivity (c), for HCP (solid lines) and VCP (dashed lines) configurations at h=1 m (in red) and h=0.3 m (in blue) clearances.

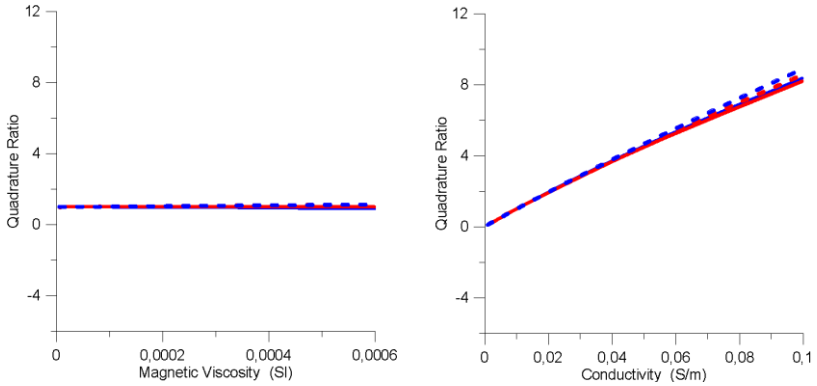

Figure 6: EM31 (L=3.66 m, f=9.8 kHz) ratio of the quadrature secondary field to the quadrature secondary field of the reference model for magnetic viscosity (a) and electrical conductivity (b), for HCP (solid line) and VCP (dashed line) configurations at h=1 m (in red) and h=0.3 m (in blue) clearances.

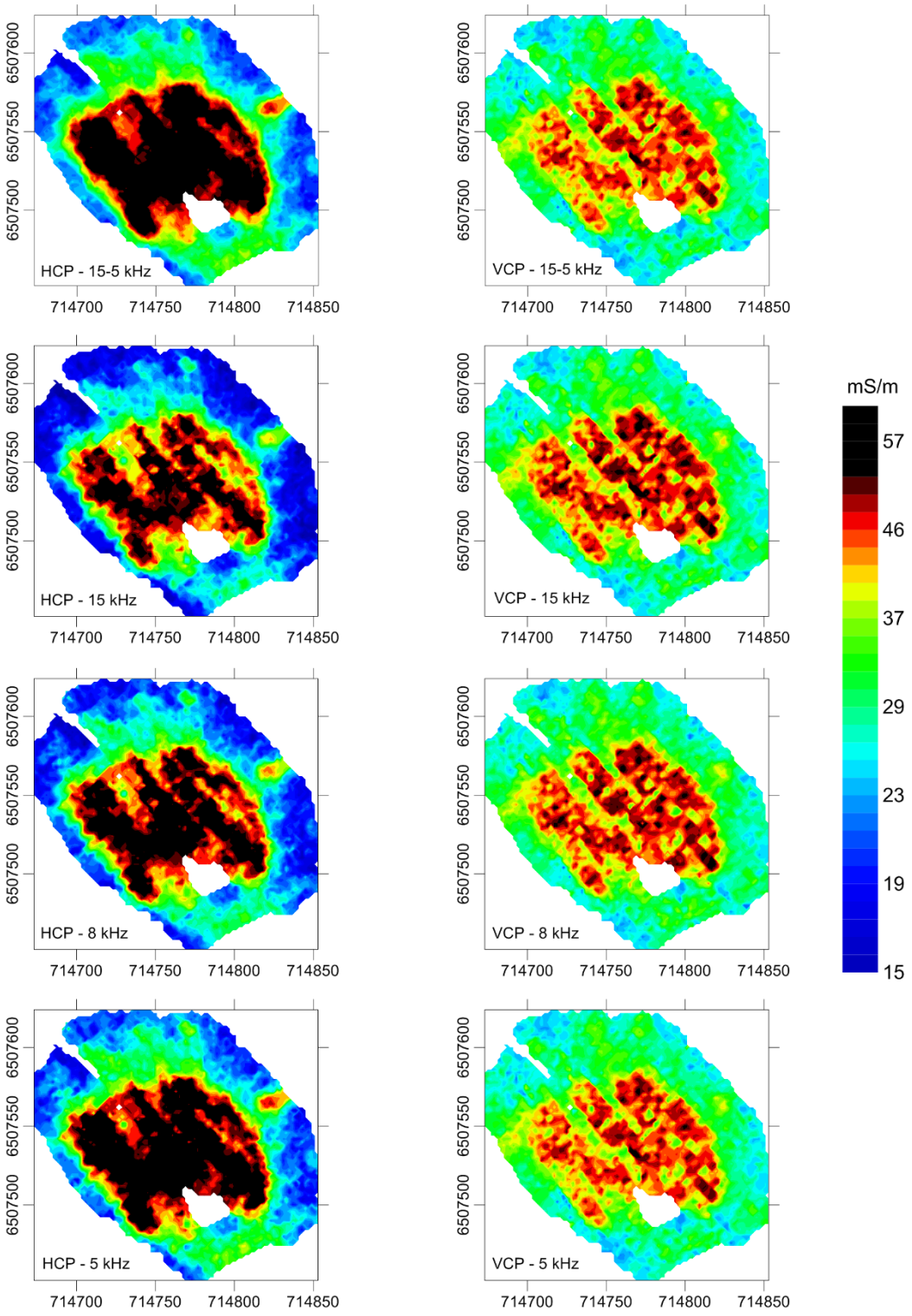

Figure 7: EMP400 apparent conductivity maps: determined using the difference in quadrature response between 15 kHz and 5 kHz (Simon et al. 2015) (above), and at each frequency (5, 8 and 15 kHz) (below).

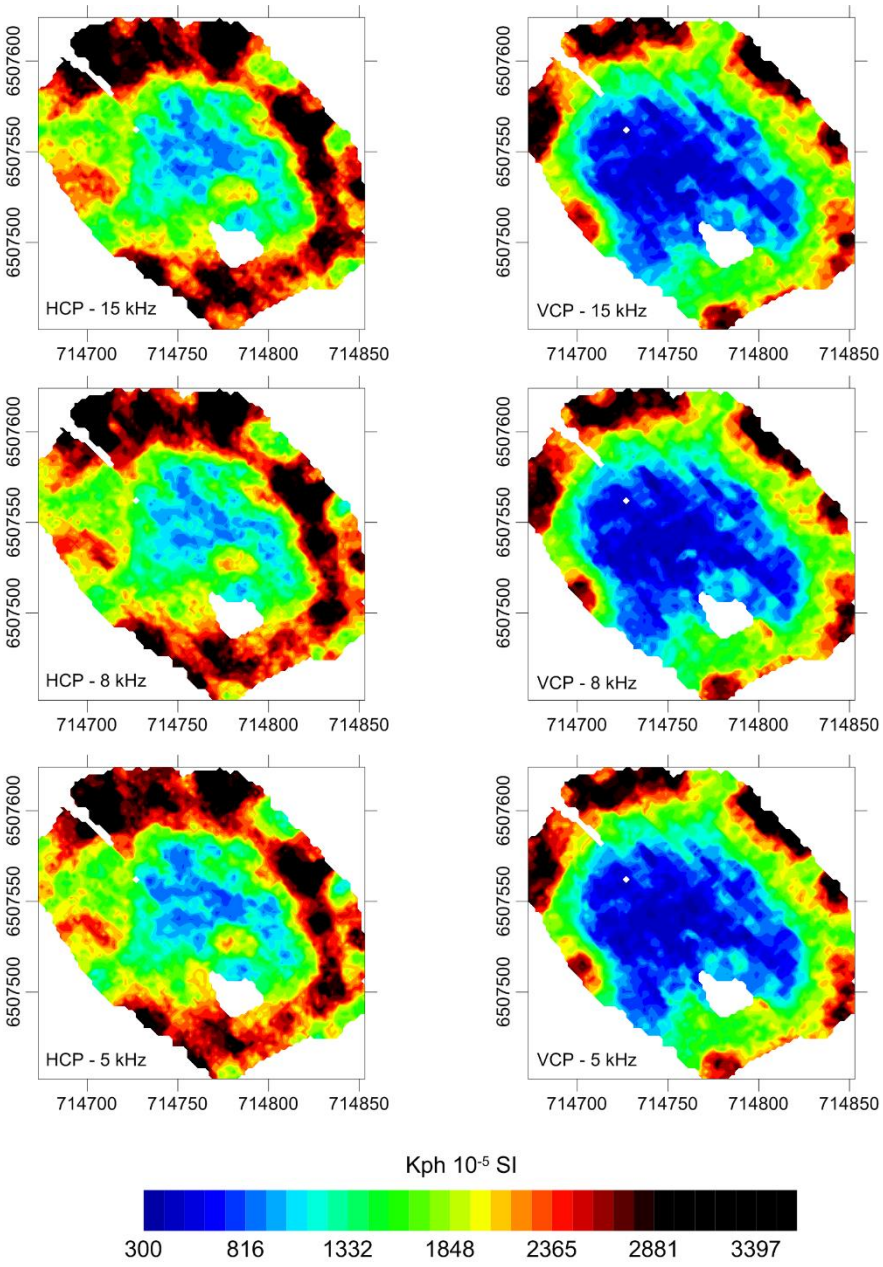

Figure 8: EMP400 apparent magnetic susceptibility maps, κ_{ph}, at the three frequencies used (5, 8 and 15 kHz), for HCP (left) and VCP (right) configurations.

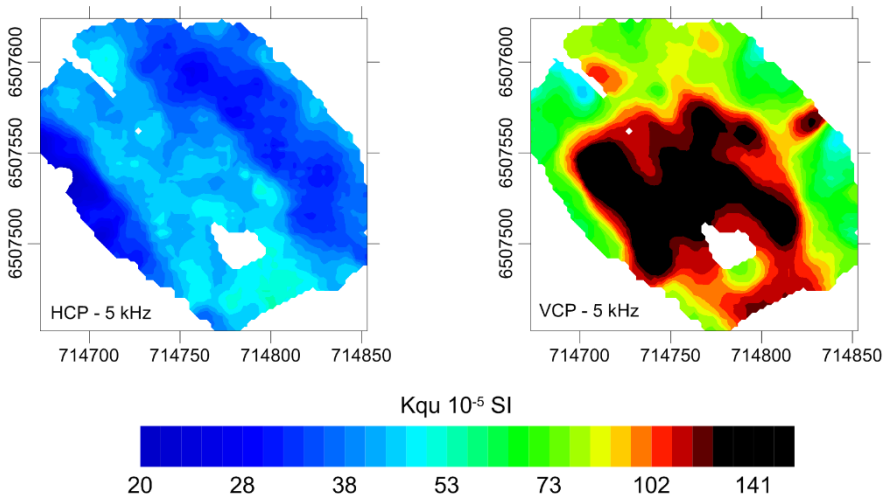

Figure 9: EMP400 apparent magnetic viscosity map κ_{qu} for HCP (left) and VCP (right) configurations.

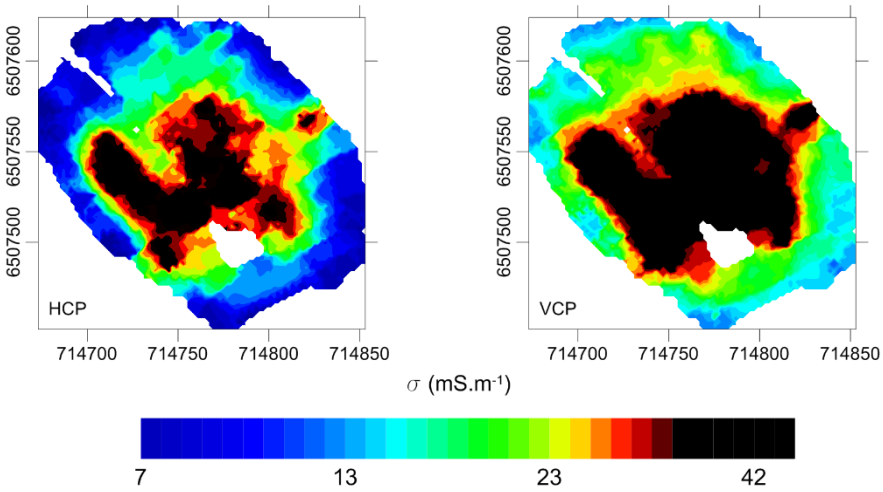

699

700 Figure 10: EM31 apparent electrical conductivity maps for HCP (left) and VCP (right)

701 configurations.

702

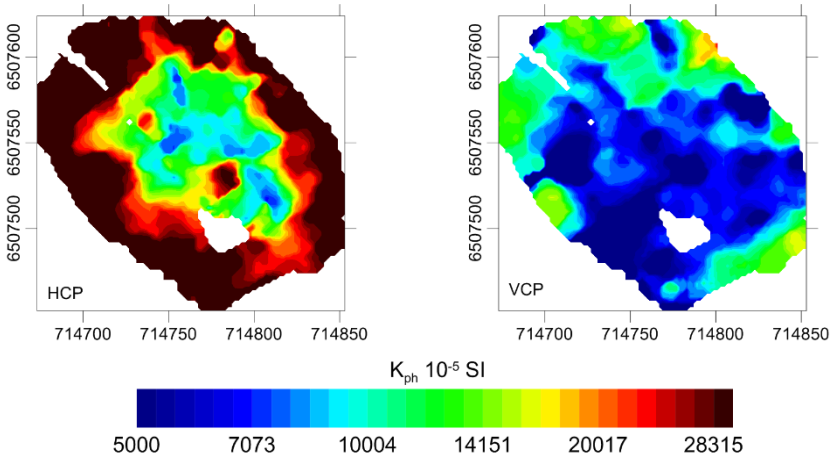

703

704 Figure 11: EM31 apparent magnetic susceptibility, κ_{ph}, maps determined without taking the

705 relative permittivity, ε_r, response into account for the HCP and VCP configurations.

706

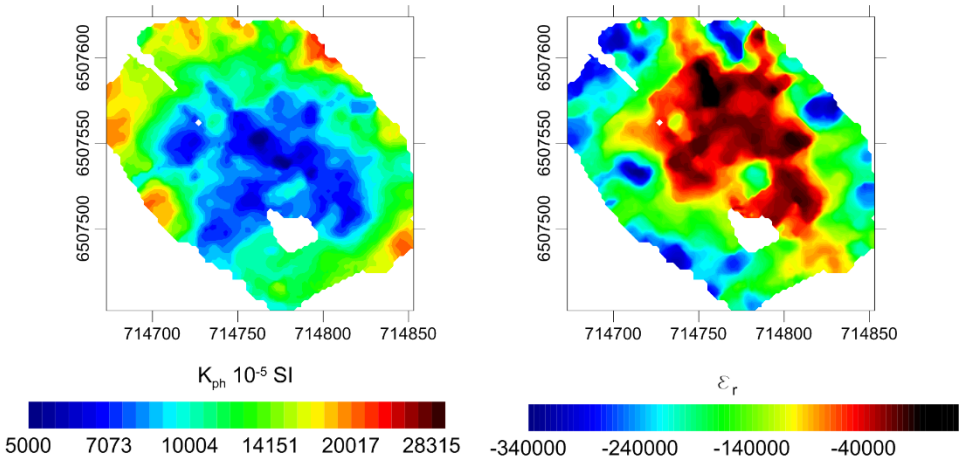

707

708

709 Figure 12: EM31 maps of the apparent magnetic susceptibility, κ_{ph}, and of the apparent relative

710 permittivity, ε_r, deduced from both in-phase HCP and VCP responses.

711

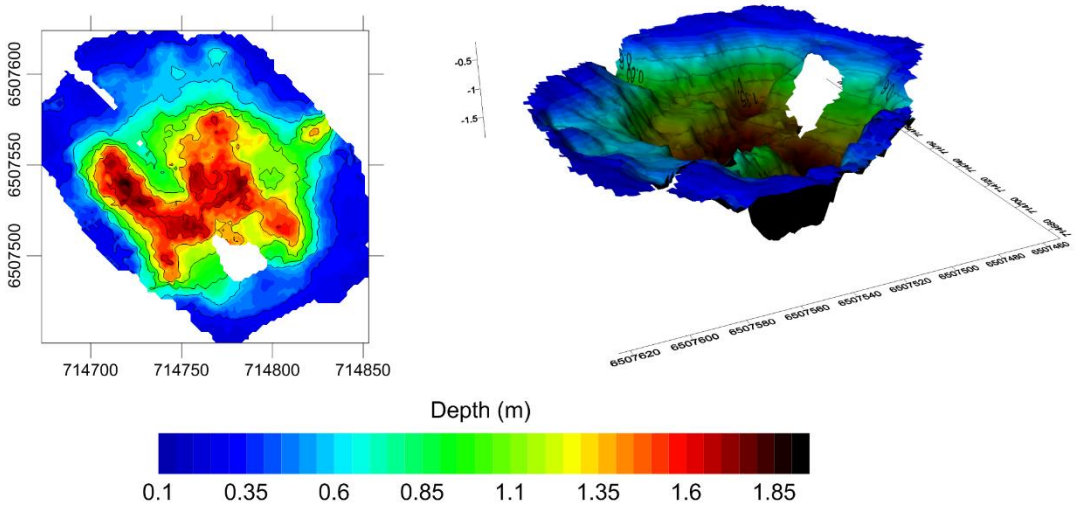

Figure 13: Thickness of the second layer, e_2, resulting from a 1D inversion when σ_1 and e_2 are variable: a) thickness map of e_2, b) oblique view of the 3D representation of e_2.

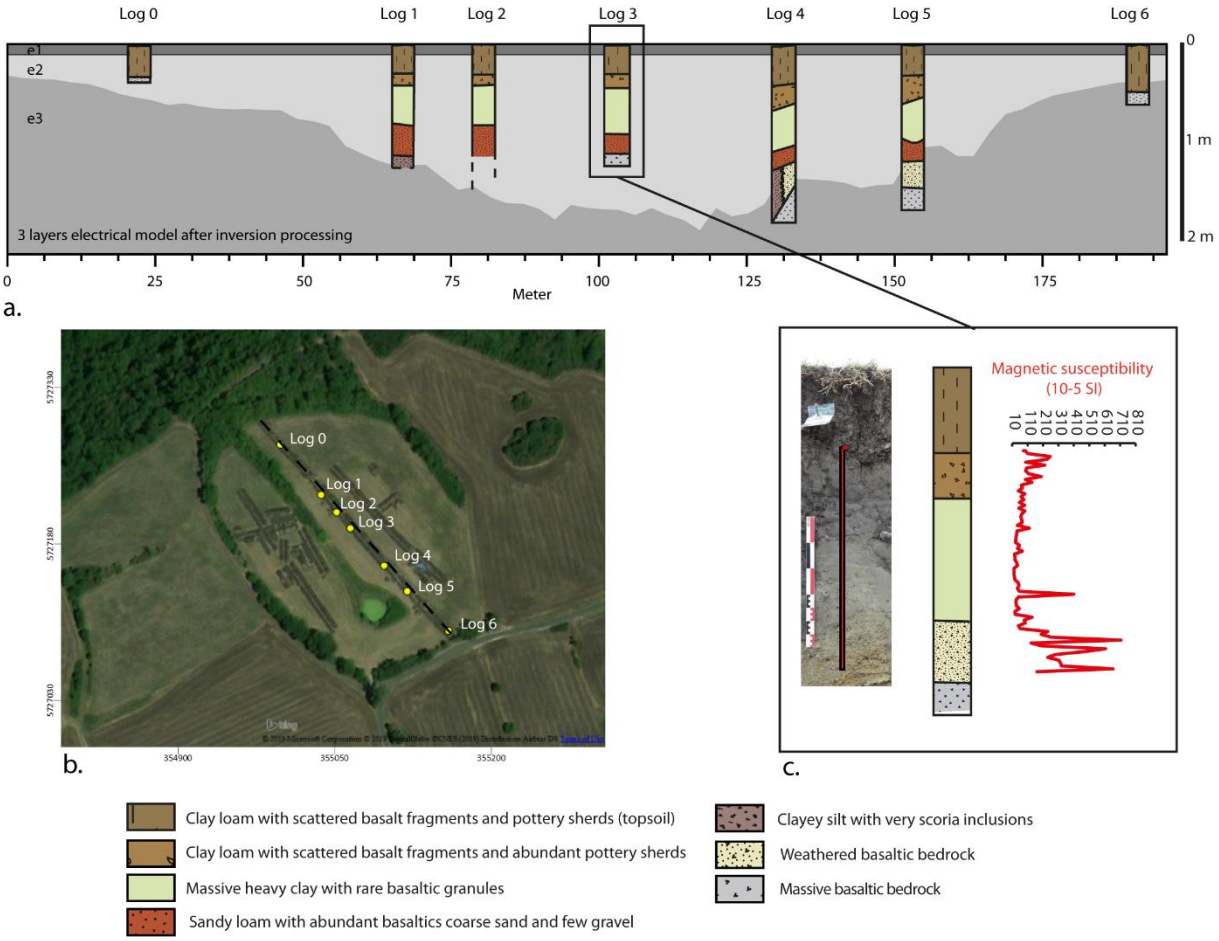

Figure 14: a) comparison of field observations and results based on the estimation of the thickness of each layer for the 3-layer model, b) location of the trench and log observation, c) Value of the magnetic susceptibility measurement of the MS2-E (Bartington Ltd) carried out on a 'U-channel' core from log 3.

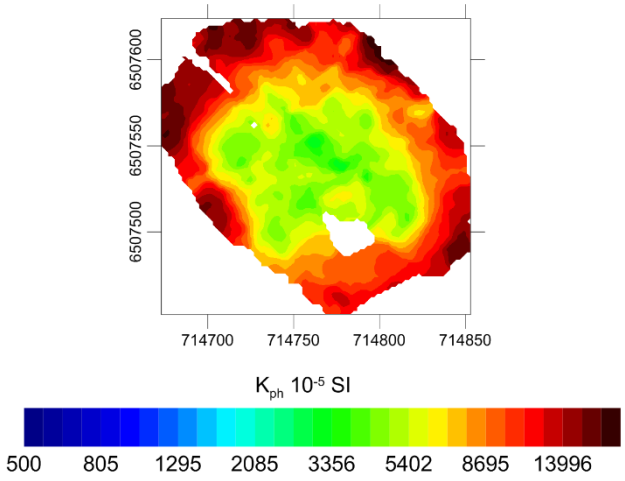

Figure 15: Inversion of the magnetic susceptibility of the second layer, ignoring permittivity variations.

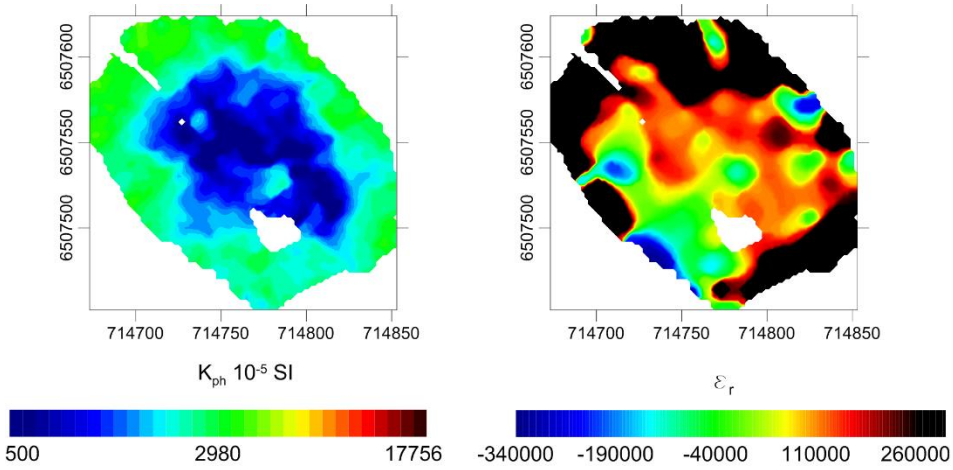

Figure 16: Inversion of both the magnetic susceptibility and the dielectric permittivity of the second layer.

EMP400	15 kHz		8 kHz		5 kHz	
	Phase	Quadrature	Phase	Quadrature	Phase	Quadrature
HCP	12500	-217	1260	20	-1300	35
VCP	-22000	-1540	-7000	-750	-3610	-500

749

750 Table 1: EMP400 zero offset corrections in ppm

751

752

In-phase EM31	1rst quartile	median	3rd quartile
VCP	75.7 ppt	82,0 ppt	93.1 ppt
HCP	32.4 ppt	42,1 ppt	52.6 ppt

753

754 Table 2: Variabilities of the in-phase EM31 raw data

755

756

EM31 (h=1m)	HCP	VCP
$\frac{\partial\left(\frac{H_s}{H_p}\right)}{\partial\varepsilon_r}$	$C_{HE=}$ 0.110 ppm	C_{VE}= 0.077 ppm
$\frac{\partial\left(\frac{H_s}{H_p}\right)}{\partial\kappa_{ph}}$	C_{HK}= -1.044 ppm/1 10^{-5} SI	C_{VK}= 3.36 ppm/1 10^{-5} SI

757

758 Table 3: Sensitivities of the EM31 in-phase responses to a homogeneous ground susceptibility

759 and permittivity when h=1 m

760

761